A New Mechanism of Light-Induced Bubble Growth to Propel Microbubble Piston Engine

Xin Yan, Jinliang Xu,* Zhijun Meng, Jian Xie, and Hao Wang

Radiation pressure refers to the momentum transfer of photons during light "particles" impacting a surface. The force is too small to drive microengines. Different from the classical radiation pressure, the indirect radiation pressure (F_m) is introduced, coming from the momentum change of light-induced bubble expansion. F_m is shown to obey $F_m \sim (I \cdot r_b)^2$, behaving faster growth of indirect radiation pressure versus light intensity I and bubble radius r_b. An effective bubble size range is identified for F_m to suppress other forces for bubble in liquid. The top laser irradiation on nanofluid is used in this experiment. A well-defined bubble pulsating flow, being a new principle of bubble piston engine, is demonstrated. During pulse on (≈ns scale), F_m exceeding other forces generates an extremely large acceleration, which is three to four orders larger than the gravity acceleration, propelling the bubble traveling downward. During pulse off, the bubble is floating upward due to the nonexistence of F_m. In such a way, the piston engine sustains the oscillating ranges of 38–347 μm for bubble diameters and 2.7–457.9 μm for traveling distances of piston. This work is useful to manipulate bubble dynamics in solar energy systems, and can find various applications in optofluidics.

1. Introduction

Radiation pressure (RP, also called light pressure) is generated due to the momentum transfer of photons when light irradiates a surface. Fundamentally, it reflects the quantum-mechanical aspect of light.[1] RP, expressed as $F_m = (R + 1)I \cdot A/c$, obeys a linear law of $F_m \sim I$, where R is the surface reflectivity, I is the light intensity, A is the project surface area, and c is the light speed.[2] Such a force is useful in large systems in astronomy and astrodynamics, which explain why comet tails face away from the sun.[3–5]

RP is suggested to activate nanoparticles for functional systems,[1,6] and it also deals with interfacial problems in which

two fluids are involved.[7,8] Ashkin and Dziedzic applied the photon momentum transfer to deform an interface toward the medium having lower refractivity.[7] Because RP is much smaller than surface tension, the interface deformation is small (≈nm scale). Delville's group demonstrated a few tens of micrometers deformation for a liquid-liquid system.[8] The interface tension is as low as ≈10^{-7} mN m^{-1}, which is almost nine orders smaller than the surface tension of air-water. RP may only be useful for high light power and an ultralow surface tension system. It is difficult to drive micrometer/sub-millimeter scale machines.[9]

Here, a new radiation pressure is introduced. This force comes from the momentum change of optothermal heating-induced bubble growth, in which light provides heat for liquid evaporation. Because the two-phase fluid is responsible for the momentum change instead of photons, we call it the indirect radiation pressure (IRP). The term "indirect" clarifies the difference between IRP and the classical RP. Even though the evaporation momentum force has been proposed and used to deal with boiling heat transfer under substrate heating conditions,[10,11] IRP, light-induced evaporation momentum force, is never mentioned in the literature. We show that IRP is scaled as $F_m \sim (I \cdot r_b)^2$, where r_b is the bubble radius. Hence, IRP is not only significantly larger, but also rises much faster with a small increase in light intensity, compared to classical RP.

We note that the light-driven nanoscale particles motion is a hot research topic. Šípová-Jungová et al.[12] reviewed the principles, realizations, and opportunities of light-driven nanomotors. The light-matter interactions can be classified into three broad classes: classical radiation pressure, photothermal heating, and photocatalysis.[9,12] The former allows nanoparticles to be trapped in a very high light intensity region of a focused laser beam (given that the real part of the particle polarizability is positive), an effect that is utilized in optical tweezers.[12] The light-nanoparticles interaction gives rise to the plasmonic effect for efficient solar energy utilization.[13] To manipulate very small bubbles, the widely used mechanism is the Marangoni effect, in which bubbles can move in a nonuniform temperature field.[14] Here, the IRP mechanism is introduced. The idea is that when light irradiates a bubble, the bubble can be divided into a sunny side and a night side. A net force is generated during the momentum change of the vapor-liquid

X. Yan, Prof. J. Xu, Z. Meng, Dr. J. Xie, H. Wang
Beijing Key Laboratory of Multiphase Flow and Heat Transfer for Low Grade Energy Utilization
North China Electric Power University
Beijing 102206, P. R. China
E-mail: xjl@ncepu.edu.cn
Prof. J. Xu
Key Laboratory of Power Station Energy Transfer Conversion and System
Ministry of Education
North China Electric Power University
Beijing 102206, P. R. China

ADVANCED
SCIENCE NEWS
www.advancedsciencenews.com

NANO · MICRO
small
www.small-journal.com

two-phase system, which is caused by symmetry breaking with the asymmetric evaporation between sunny side and night side. To the authors' knowledge, the associated mechanism is never reported in the literature.

To demonstrate the effectiveness of IRP, a light-driven boiling experiment is performed. In the system, all the forces exerted on bubble have upward direction except IRP. The latter is the only force to keep a downward direction. By using the 527 nm pulse laser, we show that IRP can balance or exceed all the other forces. Hence, bubbles never break through the air-water interface and stay underneath the water surface, breaking through the common phenomenon that vapor shall escape out of the air-water interface and enter the environment for the open boiling system. This mechanism inspires us to create a new type of bubble piston heat engine. During pulse on, IRP exceeding other forces yields a net force to propel a bubble traveling downward instantly. During pulse off, the bubble changes flow direction from downward to upward, due to non-presence of IRP. Covering the experiment data range, bubble diameters are oscillating in the range of 38–347 µm, while oscillation amplitudes of bubble displacement attain the range of 2.7–457.9 µm. These deformation parameters are at least two to three magnitudes larger than the results attained by classical radiation pressure.

2. Laser-Activated Boiling and Various Forces on A Bubble

A cuvette with an internal size of 10 mm × 2 mm × 50 mm contains a 200 ppm concentration nanofluid (see **Figure 1**a). Gold nanoparticles (NPs) have an average diameter of 17.13 nm. A 527 nm pulse laser irradiates the nanofluid from the top, having a beam diameter d_l of 368 µm. The laser irradiation creates a locally higher temperature zone ($\approx$600 µm) near air-water interface, inside which the temperature is very uniform (see Figure 1b). The higher temperature zone creates a temperature gradient along the cuvette width direction. When light intensity is low, a bulk circulation flow (BCF) is established due to the Marangoni effect on the air–water interface (see the flow field in Figure 1b), which is similar to that reported by Winterer et al.[14] Here, higher light intensities are paid more attention; under bubble oscillation occurs, being a new principle for bubble piston engine (BPE).

In this paper, four forces are analyzed, including drag force, F_d, buoyancy force, F_b, Marangoni force, F_σ, and indirect radiation pressure force, F_m. The former three have upward direction with only F_m having a downward direction (see Figure 1c). Drag force F_d is caused by shear stress between bubble and its surrounding liquid. Based on the study of Ishii and Zuber,[15] four different regimes were assumed to model F_d using different drag coefficient C_d: stokes, viscous, distorted, and churn regimes. The stokes flow with $0 < \mathrm{Re_b} < 0.2$ holds $C_d = 24/\mathrm{Re_b}$ to yield $F_d = 6\pi\mu\nu r_b$ for low Reynolds number system,[15] where $\mathrm{Re_b}$ is the Reynold number, μ is the liquid viscosity, ν is the velocity difference between an incoming stream and bubble (see Figure 1d). The buoyancy force is $F_b = 4\pi\Delta\rho g r_b^3/3 \approx 4\pi\rho_f g r_b^3/3$, where $\Delta\rho$ is the density difference between liquid and vapor, ρ_f is the liquid density, and g is the gravity acceleration.

Marangoni force occurs around a bubble in liquid. Referring to Figure 1e, a microelement area, dS, is selected on bubble surface with a microangle dφ, the Marangoni force on dS is

$$dF_{\sigma,y} = 2\pi r_b \cos^2(\varphi + d\varphi)\sigma_{\varphi+d\varphi} - 2\pi r_b \cos^2(\varphi)\sigma_\varphi \quad (1)$$

where σ is the surface tension between liquid and vapor, which is written as

$$\sigma_\varphi = \frac{d\sigma}{dT}\left|\frac{dT}{dy}\right| r_b \sin(\varphi) + C \quad (2)$$

where dσ/dT is the variation ratio of surface tension versus temperature, which is assumed to be constant, dT/dy is the temperature gradient, $C = (0.175621 T_0 + 76.5413) \times 10^{-3}$ N m^{-1}, T_0 is the liquid temperature on bubble surface at the horizontal center plane of bubble. Combining Equations (1) and (2) and integrating Equation (1) in the range of $\left[-\frac{\pi}{2}, \frac{\pi}{2}\right]$ for φ yields

$$F_\sigma = \int_{-\frac{\pi}{2}}^{\frac{\pi}{2}} dF_{\sigma,y} = -\frac{8\pi r_b^2}{3}\frac{d\sigma}{dT}\left|\frac{dT}{dy}\right| \quad (3)$$

We note that during the operation of the bubble system, the bubble is moving in a relatively uniform liquid temperature field (see Figure 1b). Thus, the assumption of linear variation of surface tension versus temperature is reasonable. Besides, Bi characterizes the relative importance of convection heat transfer with respect to conduction heat transfer: Bi = $h d_b/\lambda_f$, where h is the convection heat transfer coefficient, d_b is the bubble diameter and λ_f is the thermal conductivity of liquid. Taking the values of $h \approx 100$ W m^{-2} K^{-1} and $\lambda_f \approx 0.5$ W m^{-1} K^{-1} such as encountered in this paper, Bi $\approx$ 0.1 indicates the dominant contribution of conduction heat transfer. Heat is majorly transported via conduction in liquid for a bubble length scale to yield the linear temperature distribution in liquid.

Figure 1f,g shows the indirect radiation pressure force. For top light irradiation, a bubble has a sunny side and a night side, which are interfaced against the horizontal center plane. Because the bubble size is larger than the laser wavelength of 527 nm, light reflection I_r and refraction I_p on a bubble surface are analyzed by geometrical optics.[16] Three points are marked on the sunny side as C1 (bubble apex), C2 (critical incident angle θ_c), and C3 (margin point). The critical incident angle occurs at C2 as $\theta_c = \arcsin(n_2/n_1) = 48.75°$, where the refractive ratio is $n_1 \approx 1.33$ for water and $n_2 \approx 1$ for vapor. Light irradiates C1 without reflection and passes through C3 directly. For arc length between C1 and C2, incident light I is decupled into I_r and I_p. Alternatively, for arc length between C2 and C3, only I and I_r are involved. Both I and I_r irradiations overheat a thin boundary layer around bubble for bubble growth, which is enhanced by the NPs' plasmonic heating. NPs may be attracted by bubble interface to self-organize them on the interface.[17,18] The plasmonic heating is significantly weakened on the night side due to the shadow effect of the bubble. For a time step dt, the evaporation at bubble interface induces a mass transfer from liquid to vapor, yielding an increase in bubble volume dV. Due to bubble expansion, forces are exerted on the surrounding liquid of bubble. Correspondingly, antiforces are applied to the
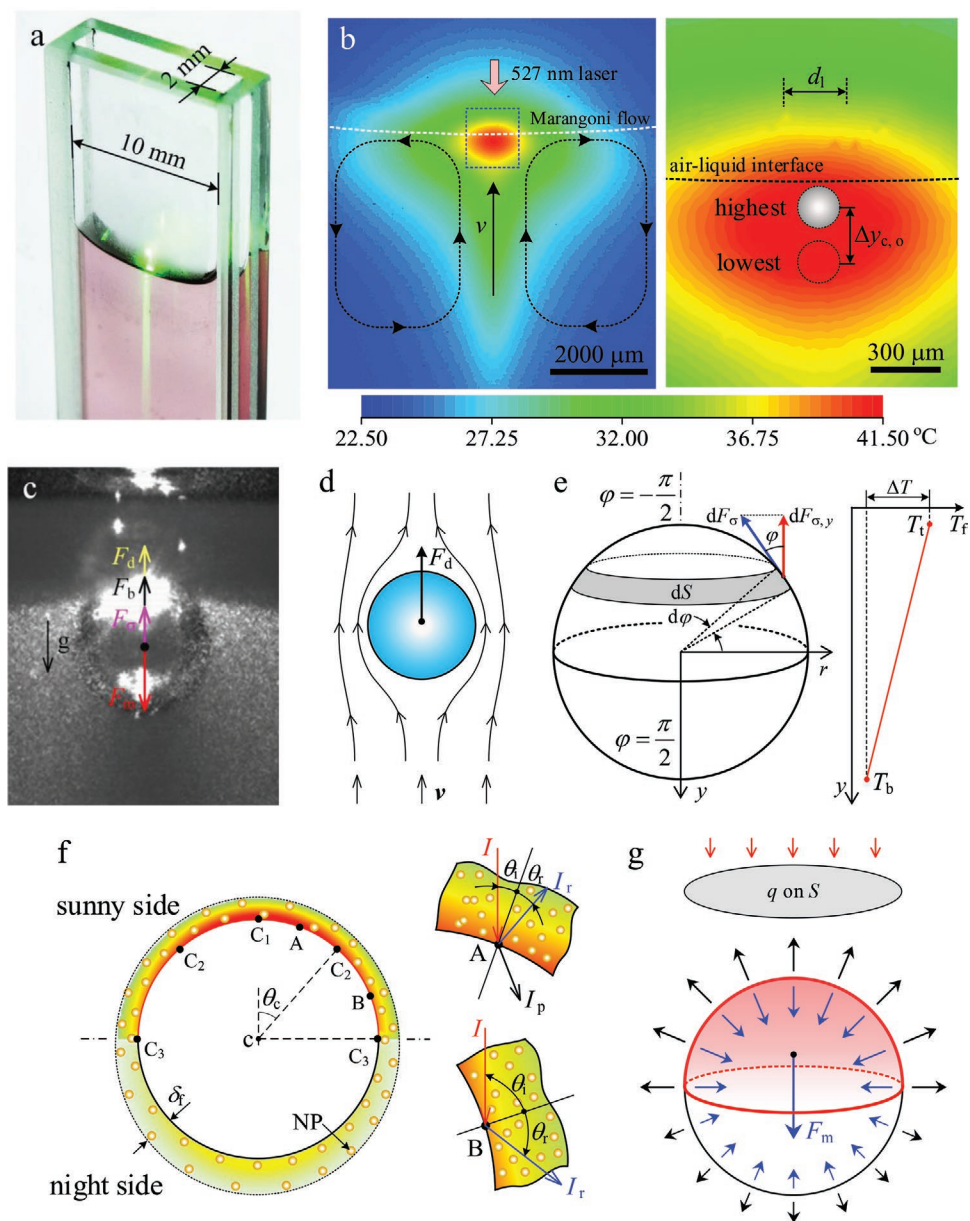
Figure 1. Test section and various forces exerted on bubble. a) The cuvette with internal sizes of 10 mm × 2 mm × 50 mm. b) Bulk circulation flow induced by temperature gradient on air–water interface; hot spot region with the uniform temperature inside. c) Photo showing strong irradiation on sunny side. d) Drag force. e) Marangoni force around a bubble. f,g) Indirect radiation pressure force.

bubble. These forces offset with each other over the horizontal plane but create a comprehensive force F_m pointing the downward direction, which is called the indirect radiation pressure. Physically, it is generated by asymmetric light energy absorption and evaporation, which is the momentum change ratio with respect to time

$$F_m = \frac{d(mv_e)}{dt} = v_e \frac{dm}{dt} + m \frac{dv_e}{dt} \qquad (4)$$

where mv_e is the bubble momentum, m is the bubble mass, v_e is the bubble expansion velocity, and t is the time. Because it is difficult to determine the heat flux distribution around bubble

interface, we assume an equivalent heat flux q on the project area of bubble for liquid evaporation, noting that q is assumed to be contributed by the sunny side only. The conservation equations of mass and energy for bubble are

$$\begin{cases} m = \rho_g \cdot \dfrac{4\pi r_b^3}{3} \\ \dfrac{dm}{dt} = \dfrac{q \cdot \pi r_b^2}{h_{fg}} \end{cases} \qquad (5)$$

where ρ_g is the vapor density and h_{fg} is the latent heat of evaporation. One notes that

$$v_e = \frac{dr_b}{dt} \tag{6}$$

Combining Equations (4)–(6) yields

$$F_m = \frac{\pi}{4\rho_g}\left(\frac{qr_b}{h_{fg}}\right)^2 \tag{7}$$

To characterize the importance of F_m related to other forces, three nondimensional parameters are defined as

$$
\begin{cases}
Rd = \dfrac{\text{indirect radiation pressure force}}{\text{drag force}} = \dfrac{F_m}{F_d} = \dfrac{q^2 r_b}{24\mu\nu\rho_g h_{fg}^2} \\[3mm]
Rm = \dfrac{\text{indirect radiation pressure force}}{\text{Marangoni force}} = \dfrac{F_m}{F_\sigma} = -\dfrac{3}{32\rho_g}\left(\dfrac{q}{h_{fg}}\right)\Bigg/\left(\dfrac{d\sigma}{dT}\left|\dfrac{dT}{dy}\right|\right) \\[3mm]
Rb = \dfrac{\text{indirect radiation pressure force}}{\text{buoyancy force}} = \dfrac{F_m}{F_b} = \dfrac{3q^2}{16\rho_f \rho_g h_{fg}^2 g r_b}
\end{cases} \tag{8}
$$

Equations (7) and (8) are newly developed for IRP and nondimensional parameters, which are useful for future analysis in this paper.

For a bubble accelerating from rest in a liquid, part of the surrounding liquid must also be accelerated, besides the bubble itself.[19] This results in an added mass force, which will be analyzed in Section 4.2.3. F_m is caused by the phase change from liquid to vapor, but the added mass force involves a virtual mass change. Thus, F_m and the added mass force are two different forces. The latter does not affect F_m.

3. Organization of Nanoparticles on Bubble Surface and Plasmonic Heating

Various nanoscale phenomena are involved in this problem, which are described as follows.

3.1. Nanoparticles Capture by Bubble

Figure 2a analyzes how NPs in the bulk fluid travel toward the bubble interface. Thermophoresis is the movement of particles in a liquid subjected to a steady temperature gradient, where the liquid molecules at the hotter region possessing higher kinetic energy drive particles toward the colder region.[20] Bulk liquid temperature is quite uniform to yield weak thermophoresis, but an overheated thermal boundary layer (δ_f) exists near bubble interface due to plasmonic heating, noting that δ_f is in ≈μm which is significantly larger than NP size. Assuming $\delta_f =$ 10 μm and temperature difference $\Delta T = 80$ K within δ_f yields a temperature gradient of 8 K μm^{-1}. Ramachandran et al.[20] showed an ≈10^{-11} N thermophoresis force for a 1.21 nm C$_{180}$ particle in an argon liquid with a temperature gradient of 4.17 K nm^{-1}. The scale law regarding particle size and temperature gradient estimates a thermophoresis force of 10^{-15} N for the present problem, which is three orders smaller than drag force $F_d \approx 10^{-12}$ N. The latter is the key mechanism to capture NPs by bubble. F_d depends on the velocity difference $v = v_l - v_c$, where v_l and v_c are the liquid velocity and bubble velocity, respectively. For a downward traveling bubble, liquid in the night side has negative v to ensure an upward F_d. Thus, the distance between NPs and bubble decreases. Similarly, for an upward floating bubble, NPs in the sunny side approach the bubble. Thus, the sunny side and night side of the bubble alternatively capture NPs in a pulsating cycle.

3.2. NPs' Stabilization on Bubble Surface

Once NPs contact the bubble interface, they must be populated there stably. A single NP is selected at the bubble apex (see Figure 2b). Various mechanisms influence the organization of NPs on bubble; among them, pressure force F_p, surface tension force F_c, and pinning force F_l have dominant contributions.[17,21] In the normal direction, the force balance is $F_p + F_c + F_l = 0$. $F_p = 2\pi\sigma(r_p \sin\theta)^2/r_b = \pi(p_0 - p_1)(r_p\sin\theta)^2$, where r_p is the NP radius, θ is the contact angle, and p_0 and p_1 are the pressures inside and outside of the bubble. F_p has an upward direction. $F_c = 2\pi r_p\sigma\sin\zeta\sin(|\theta - \zeta|)$, where ζ is the angle at the three-phase contact point with respect to the vertical direction. The overall pinning force is $F_l = 2\pi r_p\gamma(\sin\zeta)^2$, where γ is the pinning force. F_l tends to stabilize the three-phase contact line on NP surface, resisting the motion of the three-phase contact line. Fewer studies have been reported on the pinning force, which needs further investigation.[21] Both F_c and F_l tend to stabilize NPs on bubble, which are competed with F_p. Hydrophobic NPs with $\theta > 90°$ are helpful for NPs' stabilization. When NPs are closely packed, van der Waals force, electrostatic force, and Brownian movement of particles also influence the NPs' adhesion on bubble surface.[22]

3.3. Plasmonic Heating on Bubble Surface

The closely packed NPs on bubble interface result in plasmonic heating to promote bubble growth. The interaction between electromagnetic fields and free electrons in metals induces the surface plasmon resonance (SPR). When SPR is confined in a local space around an isolated NP, it is called LSPR, depending on materials and NP size.[13] Attention is paid to the light intensity decay along the optical propagation. For the nanofluid used here, the measured decay curve is shown in Figure 2c, where I and I_0 are the light intensities at the local position and the air–water interface, respectively. Three bubble regimes are involved, but we are more interested in regimes II and III, belonging to BPE. Three specific points are marked as a, b, and c in Figure 2c. In regime II, the maximum distance between air–water interface to bubble apex is 68 μm, at which I/I_0 attains 96.94%. This corresponds to about 6% decay of the F_m at $y = 68$ μm compared to that at $y = 0$, indicating the weak light decay effect on the propelling force in regime II. The situation is changed for regime III. The maximum bubble traveling distance ≈500 μm corresponds to $I/I_0 \approx 80\%$. Hence, the F_m decreases by ≈36% at the lowest position compared to that at $y = 0$, explaining the flow direction switch which is further discussed in Section 4.2.3. In summary, the present experiment involves various microscopic processes.

ADVANCED
SCIENCE NEWS
www.advancedsciencenews.com

NANO · MICRO
small
www.small-journal.com
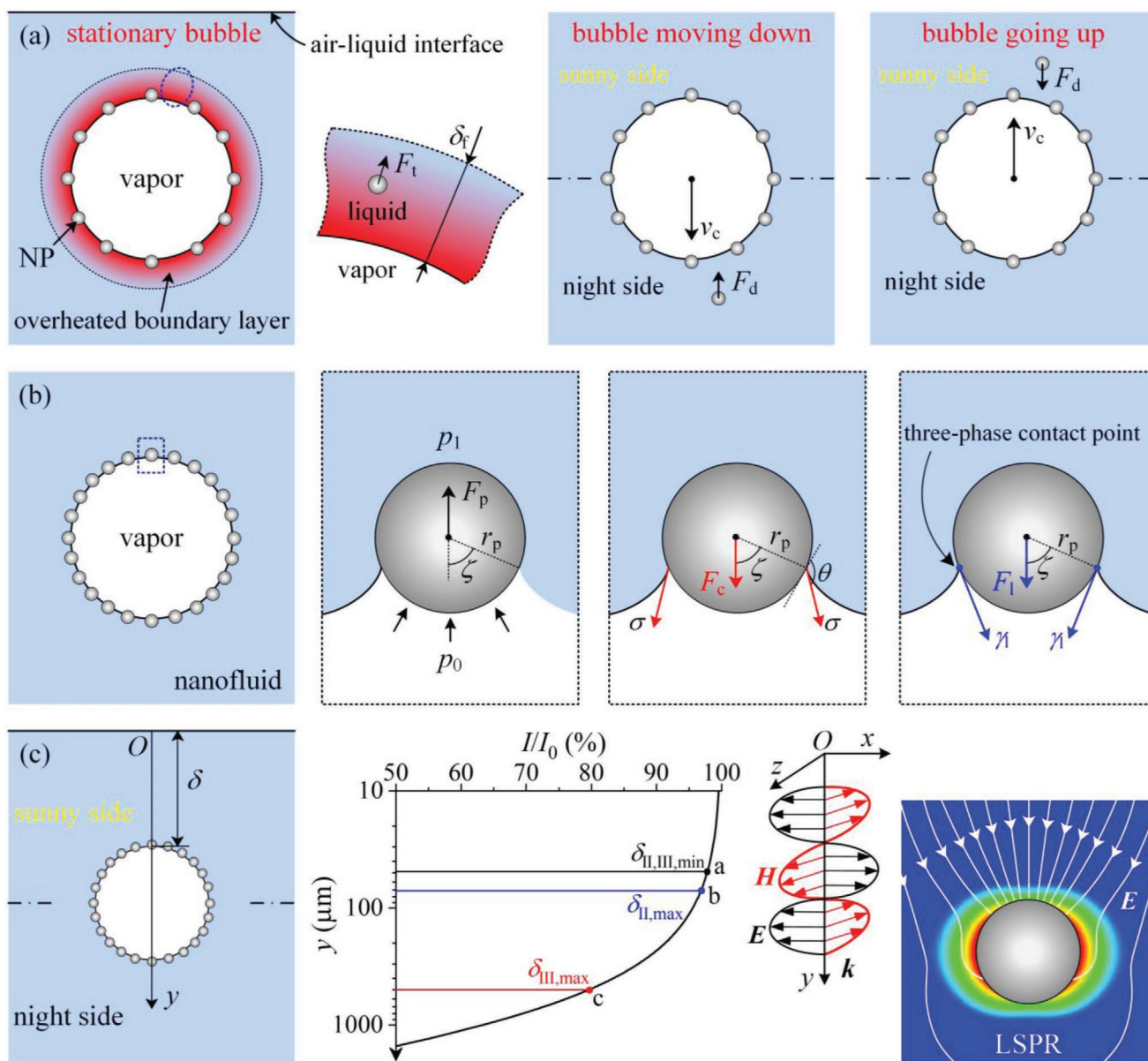
Figure 2. Organization of nanoparticles (NPs) on bubble interface and plasmonic heating. a) NPs captured by thermophoresis and drag force. b) Organization of NPs on bubble interface by pressure force, surface tension, and pinning force. c) Light intensity decay versus optical length and LSPR mechanism. The three points a, b and c have the coordinates of (48 μm, 97.83%), (68 μm, 96.94%), and (498 μm, 79.66%), respectively.

A numerical simulation linking the NPs traveling in liquid, NPs' organization on bubble interface, and plasmonic heating is difficult at this stage, but is recommended in the future. This paper focuses on the scale law analysis of various forces on bubble and demonstration of bubble piston engine.

4. Results and Discussion

4.1. Effective Bubble Sizes for Bubble Piston Engine

The scale analysis of various forces is useful to verify if the IRP can have a dominant contribution to activate the BPE. These forces are calculated for the water–steam system at 1 bar, having $\rho_g = 0.6$ kg m^{-3}, $\rho_f = 1000$ kg m^{-3}, $\mu = 0.656$ mPa s, and $h_{fg} = 2257.6$ kJ kg^{-1}. F_d needs v, which is 5 mm s^{-1} by tracking images of ≈μm bubble. One notes that both F_m and F_σ are scaled as $\sim r_b^2$, thus Rm is independent on r_b (see Equation (8)). The top light irradiation creates a higher temperature zone of ≈600 μm (see Figure 1b). The maximum diameter of bubble activity is ≈500 μm. Assuming a 0.1 K temperature difference in the 500 μm region yields dT/dy = 200 K m^{-1}, ensuring Rm ≈ 10 covering the q range in this study. This indicates the nonimportance of F_σ compared with F_m. Thus, F_σ is not considered anymore.

F_d, F_m, and F_b are shown in **Figure 3**a using a log–log plot. Because the three forces have different increase speeds versus

ADVANCED
SCIENCE NEWS
www.advancedsciencenews.com

NANO · MICRO
small
www.small-journal.com
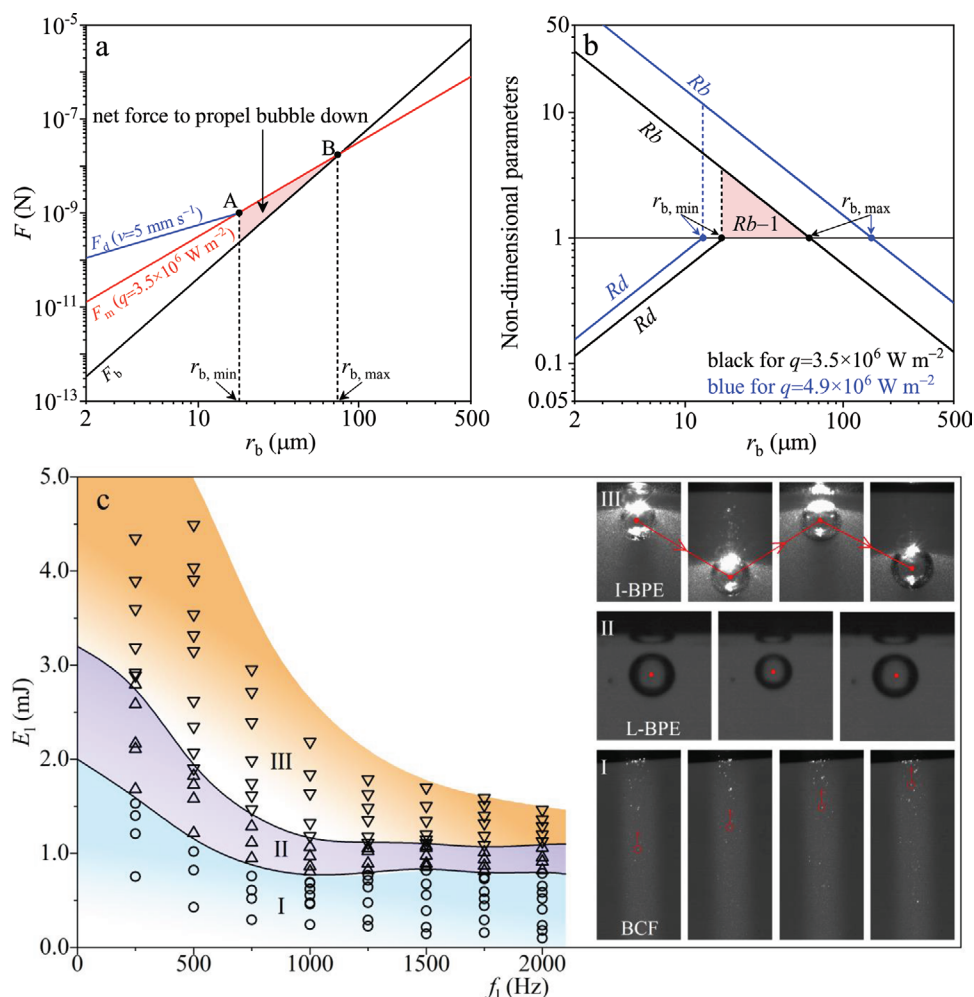
Figure 3. Scale effect of various forces with respect to bubble radii and three boiling regimes. a) Scale effect of the three competition forces. b) Scale effect of nondimensional parameters. c) Boiling regimes dependent on E_l and f_l, and regimes I, II, and III refer to bulk circulation flow (BCF), laser-frequency-controlled bubble piston engine (L-BPE), and inertia-controlled bubble piston engine (I-BPE), respectively.

bubble radii, F_m has two crossing points: one with F_d marked as A corresponding to $r_{b,min}$ and the other with F_b marked as B corresponding to $r_{b,max}$. Equation (8) and Figure 3b guide us to understand the working principle of a BPE. In the log–log plot, due to Rd and Rb scaled as $\sim r_b$ and $\sim r_b^{-1}$, the slopes of the two curves are 1 and −1, respectively. Physically, ($r_{b,min}$, $r_{b,max}$) is called the effective bubble size range to operate a BPE. For $r < r_{b,min}$, Rd is small but increases with r_b until Rd = 1 reaches at $r_{b,min}$. The imbalance force yields bulk circulation flow as shown in **Figure 4**. Within ($r_{b,min}$, $r_{b,max}$), Rd > 1 terminates bulk circulation flow of bubbles, and Rb > 1 ensures the working of BPE (see **Figures 5–7**). The pink regions in Figure 3a,b represent the net driving force $F_m - F_b$, and the nondimensional driving force Rb − 1 to propel a bubble down during pulse on, respectively. The microscopic engine stops beyond $r_{b,max}$.

Equation (7) indicates F_m scaled as $\sim (qr_b)^2$. A linear relationship between q and E_l is

$$q = \beta \frac{4E_l}{\pi d_l^2 \delta t_l} \tag{9}$$

where β is the light energy conversion efficiency, E_l, d_l, and δt_l are the single pulse energy, beam diameter, and pulse duration time, respectively. β is determined as the received energy due to bubble expansion divided by the single pulse energy

$$\beta = \frac{\rho_g \Delta V h_{fg} d_l^2}{4 r_b^2 E_l} \tag{10}$$

where ΔV is the bubble volume change during a single pulse. Taking an example with $\rho_g = 0.6$ kg m^{-3}, $\Delta V = 6.35 \times 10^{-13}$ m^3, $h_{fg} = 2257.6$ kJ kg^{-1}, $d_l = 368$ μm, $r_b = 50$ μm, and $E_l = 1.82$ mJ, one reaches $\beta = 0.63\%$. The low light energy conversion efficiency is explained by the light energy absorption by both bubble and liquid. The liquid absorption part is difficult to be considered due to a very small rise of pool liquid temperature. Here, the subcooled water at room temperature is used. The light energy conversion efficiency will increase if higher temperature liquid is used. The low light energy conversion efficiency does not influence the demonstration of BPE and major conclusions drawn in this study. Especially, F_m scaled as $\sim E_l^2$ indicates fast growth of F_m by a small rise of E_l or
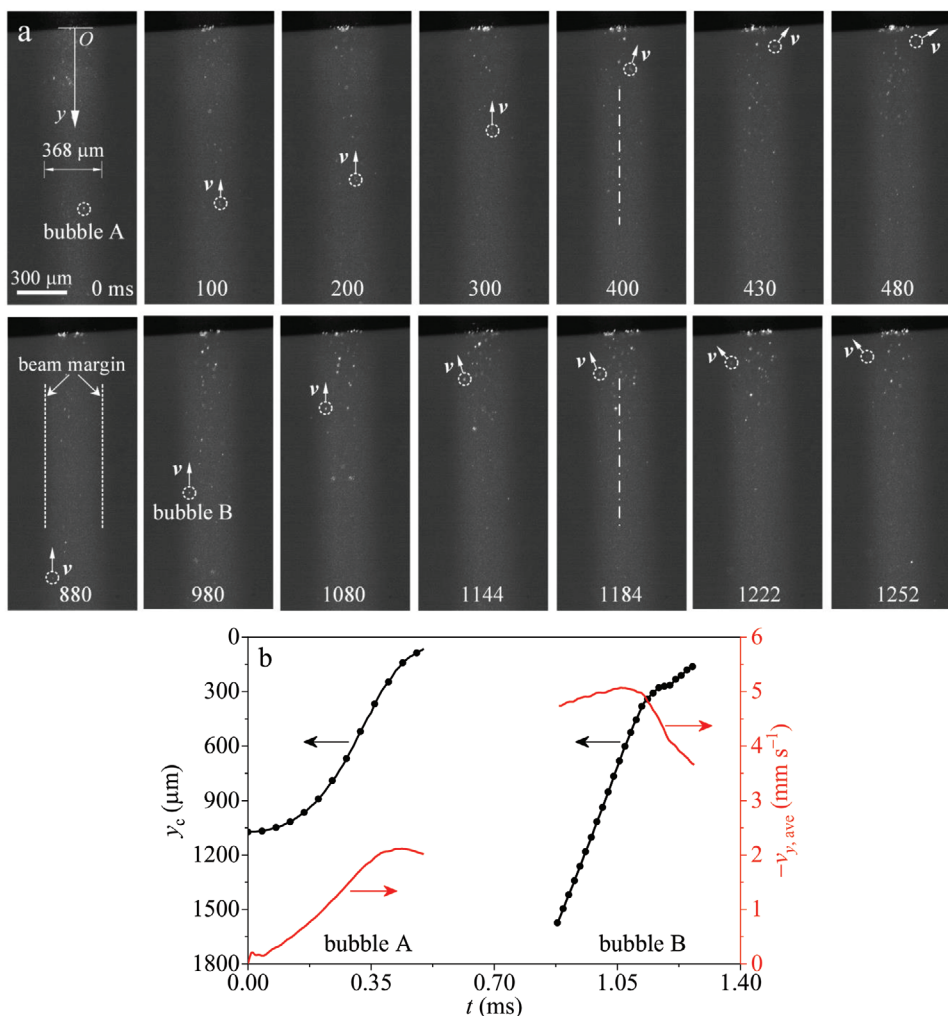
Figure 4. Regime I: bulk circulation flow. a) Rising bubbles A and B in laser beam. b) Displacement and average rising velocity versus time, $E_l = 0.8$ mJ, $f_l = 500$ Hz, and $P = 0.4$ W. The time unit is ms in panel (a).

q. This scale law enlarges the effective bubble size range, which is $r_b \in$ (17.6 µm, 61.7 µm) at $q = 3.5 \times 10^6$ W m^{-2}, but enlarged to $r_b \in$ (12.9 µm, 151.9 µm) at $q = 4.9 \times 10^6$ W m^{-2} (see Figure 3b).

Our system runs by controlling E_l and f_l, which are the two coordinates to establish a flow regime map (see Figure 3c). Regimes I, II, and III refer to BCF, laser-frequency-controlled bubble piston engine (L-BPE), and inertia-controlled

Table 1. The three regimes of laser-induced boiling in nanofluid.

Regime	$d_{b,ave}$ [µm]	$\Delta y_{c,o}$ [µm]	f_o [Hz]	f_l [Hz]	Characteristics
I	<19.0				Bulk circulation flow
II	38–329	2.7–16.3	250–2000	250–2000	Laser-frequency-controlled pulsating flow with small amplitude oscillation
III	187–347	28.3–457.9	10–106	250–2000	Inertia-controlled pulsating flow with large amplitude oscillation

bubble piston engine (I-BPE), respectively. Both L-BPE and I-BPE display bubble pulsating flow. The difference between them is that the bubble oscillation frequency f_o equals to f_l for the former, but smaller than f_l for the latter. The operation parameters and characteristics of the three regimes are summarized in **Table 1**. Figure 3c supports the scale analysis. Small E_l such as $E_l < 0.7$ mJ suppresses F_m so that Rd = 1 cannot be satisfied, belonging to regime I, but larger E_l or f_l is easier to trigger the pulsating flow, belonging to regimes II and III. At the given E_l, the increase in f_l raises the laser average energy P, which is equivalent to raise q. Thus, E_l decreases to drop the transition boundary from regime I to II.
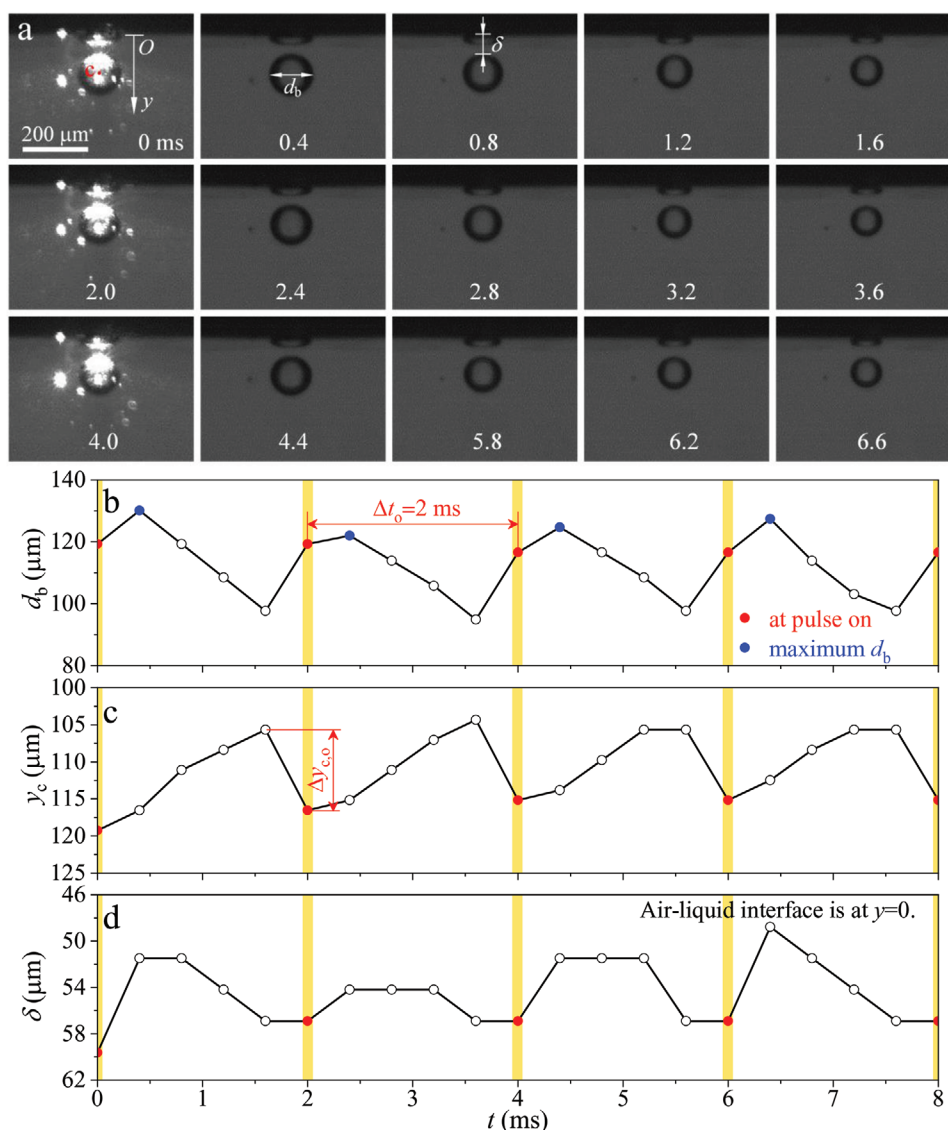
4.2. The Three Flow Regimes

4.2.1. Regime I: Bulk Circulation Flow

Bubble diameters ($d_b = 2r_b$) are ≈µm approaching the image resolution of 2.71 µm, but they can be captured

Figure 5. Regime II: laser-frequency-controlled bubble piston engine. a) Bubble images with bright images taken during pulse on, others taken during pulse off. The "c" means bubble center mass location. b–d) Periodic oscillations of bubble diameters, bubble displacement, location of bubble apex away from air–water interface, $E_l = 1.82$ mJ, $f_l = 500$ Hz, and $P = 0.91$ W. The time unit is ms in panel (a).

by a high-speed camera during pulse duration time (see Figure 4a). Laser not only provides heat for bubble nucleation and growth, but also acts as the light source for flow visualization, whose principle is identical to particle image velocimetry. Here, the ≈µm scale bubbles are the tracer particles. Bubbles are floating up in the beam, which is characterized by the average speed $v_{y,ave} = (y_t - y_{t_0})/(t - t_0)$, where t_0 is the initial time for bubble tracking (see Figure 4b). A bubble travels faster if it is closer to the beam centerline. Bubbles keep perfect upward flow direction, until they approach the air–water interface ($y < 300$ µm). Then, they make a turn, whose directions depend on their relative positions to the beam centerline. If a bubble is left to the beam centerline, it makes a left turn. Otherwise, it makes a right turn. Once bubbles are out of the light beam, they quickly disappear due to condensation by cold liquid.

4.2.2. Regime II: Laser-Frequency-Controlled Bubble Piston Engine

Pulsating flow is shown in Figure 5a, noting that white and black images are recorded during pulse on and off, respectively. Bubble dynamics are characterized by bubble diameter (d_b), bubble center displacement (y_c), and distance from water surface to bubble apex (δ, see Figure 5b–d). The pool liquid is separated by the beam into an inner warm region and an outer cold region, interfaced at the beam margin, just like a cylinder. The bubble pulsating flow in light beam is just like a piston motion in a cylinder. Based on this analogy, the pulsating flow is named as the bubble piston engine.

In each cycle, the lowest bubble position during pulse on indicates larger indirect radiation pressure F_m than buoyancy force F_b. The difference between them is the net force to propel the bubble for downward traveling. On the contrary,

ADVANCED
SCIENCE NEWS
www.advancedsciencenews.com

NANO · MICRO
small
www.small-journal.com
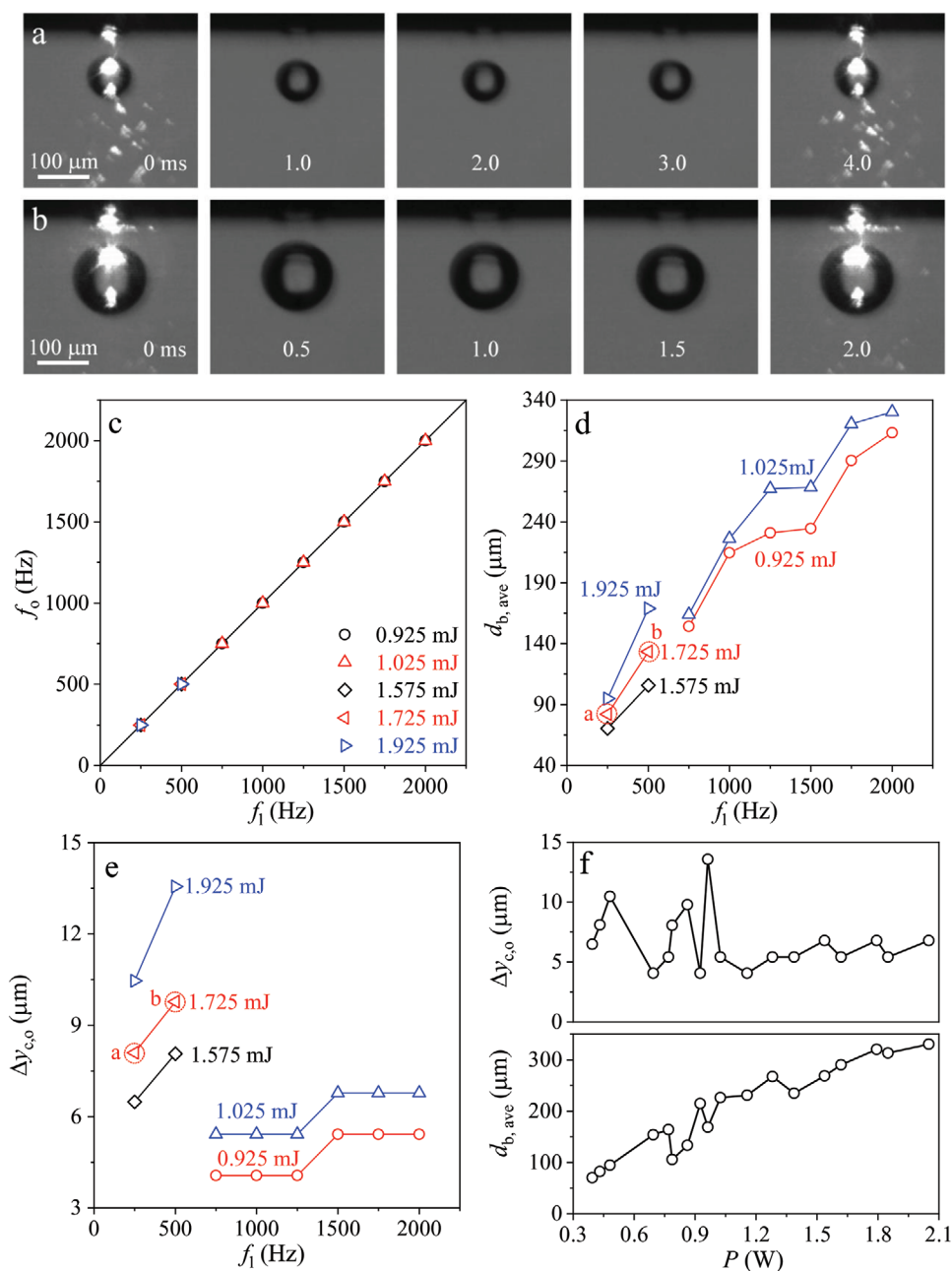
Figure 6. Effect of laser parameters on bubble oscillations. a) Bubble images in one cycle with $E_l = 1.725$ mJ and $f_l = 250$ Hz. b) Bubble images in one cycle with $E_l = 1.725$ mJ and $f_l = 500$ Hz. c) Bubble oscillation frequency equals laser pulse frequency. d) Bubble diameters dependent on E_l and f_l. e) Bubble oscillation amplitude dependent on E_l and f_l. f) Effect of P on bubble oscillation amplitudes and diameters. The time unit is ms in panels (a) and (b).

F_m disappears but F_b propels the bubble up during pulse off. It is observed that δ is oscillating in the range of 48.8–59.6 μm. In each cycle, the pulse duration holds a larger bubble but not the largest. The maximum bubble diameter occurs at 0.4 ms beyond the pulse duration. This time delay is caused by the thermal inertia of the bubble. When a pulse signal just recedes, the thermal boundary layer around the bubble is still overheated to expand a bubble. This process is related to the thermal inertia time for bubble growth τ_i[23]

$$\tau_i = \frac{(\delta_f r_b)^2}{(r_b - \delta_f)^2 \pi \alpha_d} \tag{11}$$

where δ_f is the overheated thermal boundary layer thickness and α_d is the thermal diffusion coefficient of liquid. Based on Equation (11), the inertia time of 0.4 ms corresponds to the δ_f of 11 μm, which continuously supplies the energy for bubble expansion. This estimation explains why the bubble is the largest after 0.4 ms beyond pulse duration.

ADVANCED
SCIENCE NEWS
www.advancedsciencenews.com

NANO · MICRO
small
www.small-journal.com
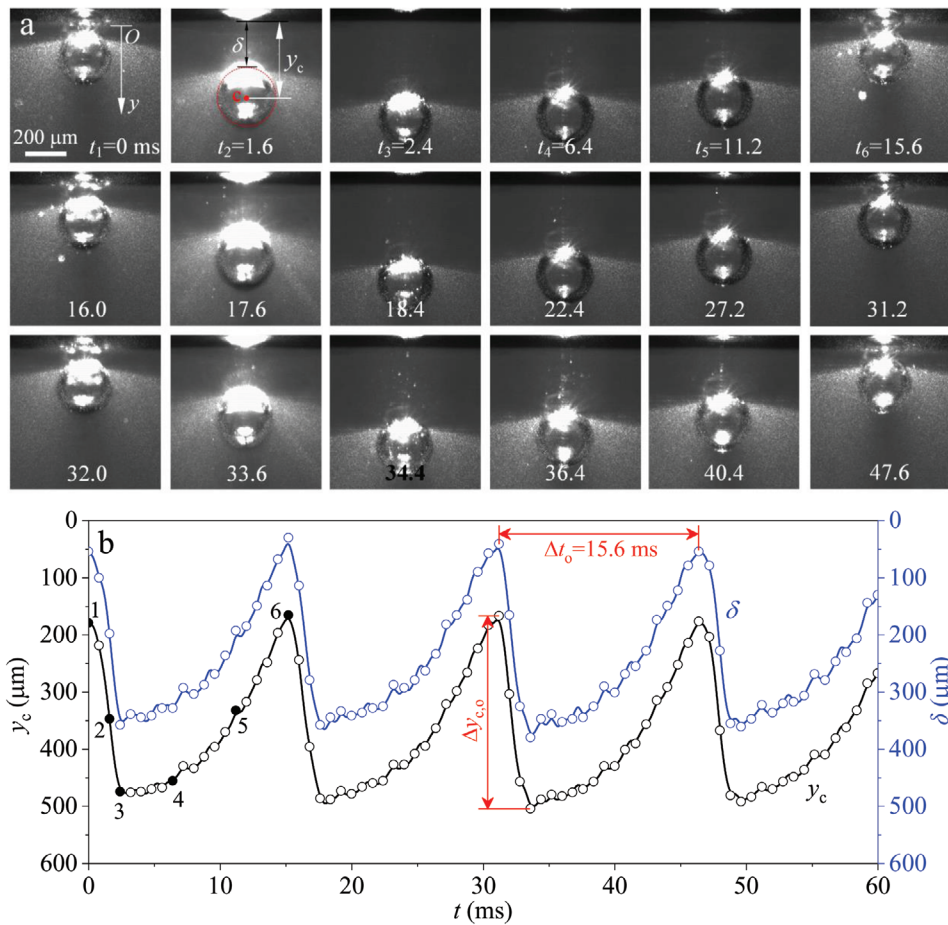
Figure 7. Regime III: inertia-controlled bubble piston engine. a) Images showing pulsating flow. b) y_c and δ versus time with $E_l = 2.4$ mJ, $f_l = 500$ Hz, and $P = 1.2$ W. The studied case had $\Delta t_o = 15.6$ ms and $\Delta y_{c,o} = 337.3$ µm. The time unit is ms in panel (a).

In regime II, f_o is equal to f_l. Thus, it is called the laser-frequency-controlled engine, which is verified over a wider range of $E_l = 0.925$–1.925 mJ and $f_l = 250$–2000 Hz (see Figure 6a–c). The bubble diameters averaged between maximum and minimum ($d_{b,ave}$) increase with increases in E_l and f_l (see Figure 6d). The increased $d_{b,ave}$ by P is explained by nonequilibrium heat transfer of bubble in liquid. When laser irradiates nanofluid, the increase in P enhances nanoparticles' plasmonic heating, supplying more heat to thermal boundary layer for bubble growth. Simultaneously, the bubble is condensed by the subcooled liquid, dependent on the temperature difference between saturation vapor and subcooled liquid. The increase in P elevates the temperature level of subcooled liquid, weakening the condensation effect. Thus, by increasing E_l or f_l, both effects raise q to increase $d_{b,ave}$ (see Figure 6d).

The oscillation amplitude of piston engine characterizes the maximum traveling distance of a bubble in light ($\Delta y_{c,o}$), which attains 4.1–13.6 µm covering the E_l and f_l ranges in this regime. Figure 6e shows the effects of E_l and f_l on $\Delta y_{c,o}$, indicating either the increasing trend versus f_l at larger E_l or not sensitive to f_l at smaller E_l. During pulse on, Newton's second law writes

$$F_m - F_b = (Rb-1) F_b = ma \tag{12}$$

where the left-hand side of Equation (12) is the net force for bubble traveling down and a is the bubble acceleration. Substituting F_b and m in Equation (5) into Equation (12) yields

$$a = (Rb-1) \cdot \frac{\rho_f}{\rho_g} \cdot g \tag{13}$$

where ρ_f/ρ_g is the density ratio between liquid and vapor, and $(Rb-1) \cdot \rho_f/\rho_g$ is called the amplification factor with respect to the gravity acceleration g. Thus, a is significantly large, for example, $a = 1.47 \times 10^5$ m s^{-2} at $Rb = 10$, which is $\approx 10^4$ times of g. Assuming the acceleration motion with constant a during pulse duration, $\Delta y_{c,o}$ is scaled as

$$\Delta y_{c,o} \sim \frac{(Rb-1)}{2} \cdot \frac{\rho_f}{\rho_g} \cdot g \cdot \delta t_l^2 \tag{14}$$

Equation (14) indicates $\Delta y_{c,o} \sim (Rb-1)$ and Equation (8) shows $Rb \sim q^2/r_b$. Thus, a positive effect and a negative effect simultaneously exist regarding the influence of P on $\Delta y_{c,o}$. First, the increase in P raises q, elevating Rb and $\Delta y_{c,o}$ according to the scale law of $\sim q^2$. This is a positive effect. Second, the increase in P raises r_b (see Figure 6d,f), suppressing $\Delta y_{c,o}$ according to the scale law of $\sim r_b^{-1}$. This is a negative effect. The competition between the two effects yields the nonmonotonic variation trend regarding the effects of

ADVANCED
SCIENCE NEWS
www.advancedsciencenews.com

NANO · MICRO
small
www.small-journal.com

E_l, f_l, and P on $\Delta\gamma_{c,o}$ (see Figure 6e,f). Figure 6e shows a sudden decrease of $\Delta\gamma_{c,o}$ for $E_l = 1.025$ and 0.925 mJ. Due to $\Delta\gamma_{c,o} \sim E_l^2$, $\Delta\gamma_{c,o}$ should be smaller for $E_l = 1.025$ and 0.925 mJ compared to other E_l curves. Besides, even though the two E_l values are smaller, the higher frequency operation increases the laser power to increase the pool liquid temperature, weakening condensation between bubble and liquid. This effect increases the bubble size r_b to further decrease the oscillation amplitudes according to $\Delta\gamma_{c,o} \sim r_b^{-1}$.

4.2.3. Regime III: Inertia-Controlled Bubble Piston Engine

Regime II involves smaller bubble sizes with $d_b = 38$–329 μm. Further increase in laser energy generates larger bubble, which contacts light margin, belonging to regime III. Light irradiation generates a bubble inertia velocity $v_{c,i}$ at the end of pulse duration. When the pulse signal recedes, the bubble continues to travel downward until $v_c = 0$ is reached. In the deceleration process, F_d is not considered due to $F_d \ll F_b$. Besides the bubble itself, the surrounding liquid is also moving.[19] This gives rise to an added mass force having downward direction, which is competed with the buoyancy force in an upward direction

$$\frac{4}{3}\pi r_b^3 \rho_f C_m \frac{dv_c}{dt} \sim \frac{4}{3}\pi r_b^3 \rho_f g \tag{15}$$

where v_c is the bubble velocity at t. The left-hand side and the right-hand side of Equation (15) are added mass force and buoyancy force, respectively. C_m is the added mass coefficient, $C_m = 0.5$, for a spherical bubble in an infinite domain.[19] Equation (15) gives

$$\frac{dv_c}{dt} \sim \frac{g}{C_m} \tag{16}$$

Equation (16) yields the characteristic time of bubble inertia scaled as $\Delta t_i \sim C_m v_{c,i}/g$. Thus, Figure 5 for regime II indicates the laser-frequency-controlled pulsating flow due to $\Delta t_i = 1.35$ ms $< 1/f_l = 2.0$ ms, but Figure 7 for regime III presents the inertia-dominated pulsating flow due to $\Delta t_i = 9.8$ ms $> 1/f_l = 2.0$ ms. Regime III maintains a larger bubble size ($d_b \approx d_l$) and displays a larger oscillation amplitude such as $\Delta\gamma_{c,o} = 337.3$ μm. A pulsating cycle includes an immersing stage and a floating stage. In each cycle, a bubble may be irradiated by a set of pulse signals. Now that the F_m is exerted on the bubble several times during its downward traveling, how to fulfill the flow direction switch? This question is related to a feedback effect regarding the light intensity decay along the optical propagation. When the bubble is closer to the air–water interface, the light irradiation causes a larger F_m for downward traveling. However, when the immersion depth increases, the effective light intensity for bubble irradiation slightly decreases. This gives rise to an obvious decrease in F_m due to the scale law of $F_m \sim I^2$. When the bubble travels to a specific depth, F_m can be smaller than F_b, so that the bubble turns to float toward the water surface. Examining Figure S1 (Supporting Information) helps to understand this feedback mechanism.

4.3. Transition between Different Regimes

In regime I, dispersed bubbles are traveling upward in light. These bubbles ($d_b = 3$–19 μm) are too small to satisfy the criterion

Rd > 1. In regimes II and III, only a single but larger bubble displays pulsating flow. The transition between different regimes is paid attention here. The run with $E_l = 1.08$ mJ and $f_l = 500$ Hz in regime II approaches the transition boundary from regime I to II (see Figure 3c). The transition occurs due to the coalescence of bubbles (see **Figure 8**a). Bubbles B1 and B2 are mixed to form B3. Then, bubbles B3 and B4 are mixed to form B5. This process continues until a larger bubble is generated at $t = 306.5$ ms to terminate bulk circulating flow but sustains pulsating flow.

Figure 8b demonstrates how a bubble enlarges its size during the transition from regime II to III. At $t = 341.0$ ms, a larger bubble is defined as the mother bubble. Due to stronger light irradiation, a smaller bubble, called daughter bubble, can be nucleated and grow on the night side of the mother bubble. The coalescence of the two bubbles enlarges the mother bubble size (see images at $t = 341.0$–348.5 ms). Before the coalescence, the surface energies of the two bubbles are

$$E_m = 4\pi\sigma r_{b,m}^2, \quad E_d = 4\pi\sigma r_{b,d}^2 \tag{17}$$

The merged bubble has the surface energy of

$$E_n = 4\pi\sigma r_{b,n}^2 = 4\pi\sigma \left(r_{b,m}^3 + r_{b,d}^3\right)^{2/3} \tag{18}$$

In Equations (17) and (18), the subscripts m, d, and n represent the mother bubble, daughter bubble, and newly merged bubble, respectively. The residual energy after coalescence E_r is

$$E_r = E_m + E_d - E_n = 4\pi\sigma\left[r_{b,m}^2 + r_{b,d}^2 - \left(r_{b,m}^3 + r_{b,d}^3\right)^{2/3}\right] > 0 \tag{19}$$

Assuming $r_{b,m} = 2r_{b,d}$ reaches a new bubble radius which is 6% larger than the mother bubble, and achieves a residual energy of 33.5% of the mother bubble's surface energy, part of the residual energy is converted into kinetic energy, triggering the bubble to travel downward (see images at $t = 355.5$–364.0 ms). This phenomenon is called the "bubbles-coalescence-induced-jumping," which is analogized to the droplets-coalescence-induced-jumping.[24] For comparison, the bubble jumps downward against the buoyancy force direction, but droplet jumps upward against the gravity direction. The bubbles-coalescence-induced-jumping is an auxiliary mechanism, except the IRP, to propel the bubble down in the transition stage. For steady oscillation, jumping does not occur due to only one bubble in light. Figure 8c shows the bubble center displacement γ_c, including an initial laser-frequency-controlled pulsating stage with $\Delta\gamma_{c,o} \approx 8$ μm, a transition stage, and a final inertia-controlled pulsating stage with $\Delta\gamma_{c,o} \approx 270$ μm. Movies S1–S5 for regimes I–III, as well as the transition images, are available in the Supporting Information.

4.4. Comments and Perspective

Indirect radiation pressure is different from classical radiation pressure in the following ways. First, indirect radiation pressure comes from the momentum change of evaporation from liquid to vapor, while classical radiation pressure is caused by the momentum change of photons when light "particles"
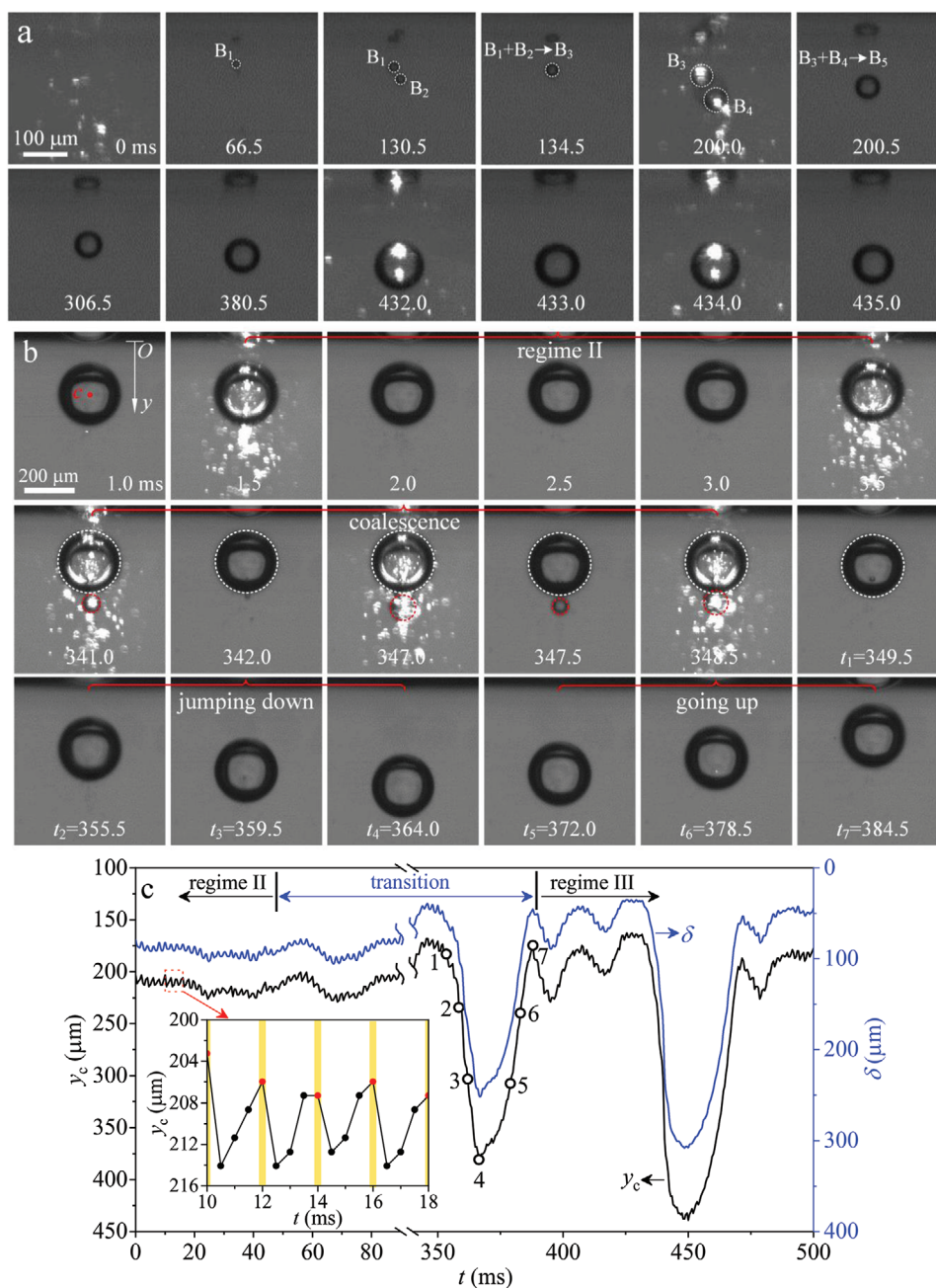
Figure 8. Transition between different regimes. a) Transition from regime I to II with $E_l = 1.08$ mJ and $f_l = 500$ Hz. b,c) Transition from regime II to III with $E_l = 2.04$ mJ and $f_l = 500$ Hz. The time unit is ms in panels (a) and (b).

impact a surface. Thus, the two radiation pressures are different in mechanisms. Second, indirect radiation pressure obeys the square law of light intensity, but classical radiation pressure is linearly proportional to light intensity. Our current work can be extended to other working fluids except water. The effects of some physical properties are mentioned here. The latent heat of evaporation, h_{fg}, is important to affect Rb and Rd (see Equation (8)). The usage of low h_{fg} fluid increases Rb and Rd, making a steam engine more actively. Because the bubble acceleration during pulse duration (a) is scaled as $\sim \rho_f / \rho_g$, the fluid with a larger density ratio between liquid and vapor

results in an enhanced piston motion (see Equation (13)). The bubble piston engine does not work using the thermocapillary effect. Thus, surface tension is not important for steady oscillation, but may influence the residual energy release during the transition between different regimes. Saturation temperature of vapor, T_{sat}, is not included in Rb and Rd, but it influences the engine working. This is because the decrease of T_{sat} decreases the temperature difference between T_{sat} and surrounding liquid, so that condensation during pulse off is weakened.

We comment on applications of BPE. Because light is a clean and contactless energy source, optofluidics has become

**ADVANCED
SCIENCE NEWS**
www.advancedsciencenews.com

NANO · MICRO
small
www.small-journal.com
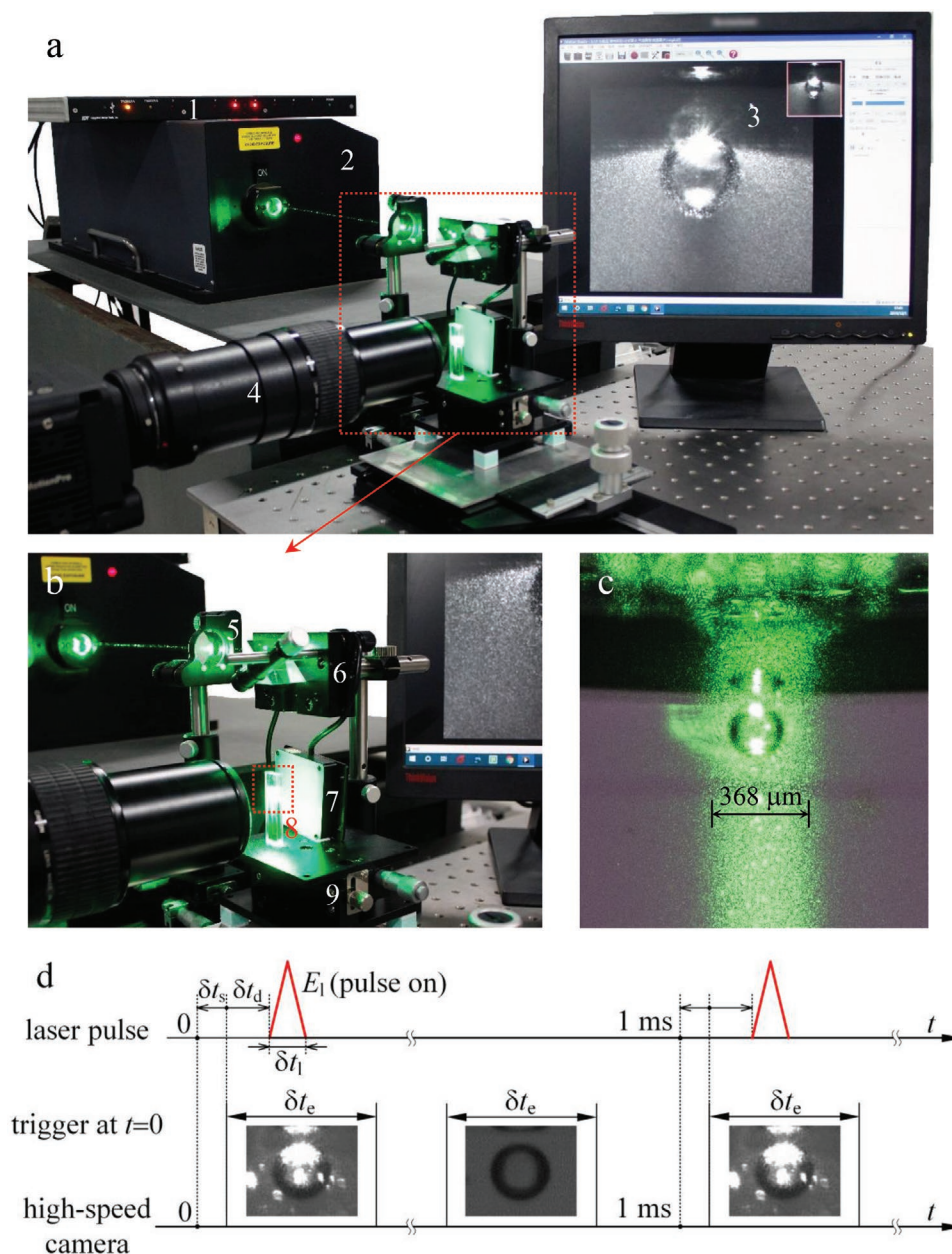
Figure 9. Experiment setup. a) 1, synchronizer; 2, 527 nm pulse laser; 3, PC screen; and 4, high-speed camera. b) 5, Focusing lens; 6, reflecting prism; 7, back light; 8, cuvette containing nanofluid; 9, three-axis displacement platform. c) Bubble observed due to optothermal heating. d) The synchronized time series combining laser and the high-speed camera, an example given for f_l = 1000 Hz, f_r = 2000 Hz, δt_s = 20 ns, δt_d = 1 µs, δt_l = 180 ns, and δt_e = 200 µs, where f_l, f_r, δt_s, δt_d, and δt_e are the pulse frequency, image capture frequency, synchronization error, pulse laser on delay, pulse duration time and exposure time of the camera, respectively.

an attractive field.[25–27] Our work adds a new principle for optofluidics. For example, due to strong mass and energy exchange between the oscillating bubble and surrounding liquid, BPE can be used in biomedical field to promote mixing and chemical reactions for different species, which have a high requirement for cleanliness.[28] Especially, the chemical reaction in a microchannel is very difficult due to the weak mixing in low Reynolds number system.[28,29] The BPE provides a strong disturbance for mixing enhancement to promote chemical reaction. Besides, pulsating flow is an approach for heat transfer

enhancement, in which reciprocating flow is necessary.[30,31] Micro-BPE fulfilled in microchannel can be a pumping source to create the reciprocating flow. Periodic bubble expansion and contraction are the principle to fabricate micropumps or valves.[32,33] Light-activated pumps and valves can be a new family of such microsystems. Recently, optofluidics has been introduced for energy applications.[34] For solar energy utilization, an active field is to produce clean vapor for power generation. IRP is expected to manipulate bubble dynamics, so that the solar-driven steam system becomes more effective.

**ADVANCED
SCIENCE NEWS**

www.advancedsciencenews.com

NANO · MICRO

small

www.small-journal.com

5. Conclusions

The asymmetric optothermal heating-induced bubble growth in a liquid causes a net force pointing the light prorogation direction, which is called the indirect radiation pressure. Our work indicates the scale law of $F_m \sim (q r_b)^2$. A group of nondimensional parameters is defined to quantify the importance of indirect radiation pressure related to other forces. Within a bubble size range, the indirect radiation pressure is not only larger than the drag force, but also larger than the buoyancy force.

A pulse laser-activated pool boiling experiment is performed, in which the nanoparticles plasmonic effect promotes the light energy absorption. Depending on single pulse energy and laser frequency, three regimes are identified: regime I for bulk circulation flow, regime II for laser-frequency-controlled bubble piston engine, and regime III for inertia-controlled bubble piston engine. Both regimes II and III display the periodic growth/contraction and oscillation of a single bubble in light beam, just like the periodic motion of a solid piston in a cylinder. Combining regimes II and III, bubble diameters are oscillating in the range of 38–347 µm, and oscillating amplitudes attain the range of 2.7–457.9 µm. Bubbles in pulse duration time keep extremely large acceleration, which is three to four orders larger than the gravity acceleration. The characteristic inertia time of bubbles determines if the bubble piston engine can be controlled by laser frequencies.

Our experiment supports the theoretical analysis regarding the scale effect of various forces on a bubble. At lower light intensity, bulk circulation flow is sustained due to smaller indirect radiation pressure than drag force. Once light energy increases, the coalescence of miniature bubbles forms a larger bubble, under which the subtraction of indirect radiation pressure from buoyancy force is the net force to drive the bubble down during pulse on. Regulating laser parameters that effectively control the effective bubble size range, the bubble diameter can even approach the beam diameter.

6. Experimental Section

The experiment was implemented on an optical platform (see **Figure 9**a). A laser device (Pegasus PIV XR, New Wave) emitted a $\lambda = 527$ nm pulse beam, which was focused by a convex lens with a focal length 160 mm. A reflection prism received light and changed its direction from horizontal to vertical. Nanofluid was irradiated by laser from the top (see Figure 9b). The Rayleigh length $L_r = 0.25 \pi d_l^2/\lambda = 119.3$ mm was two magnitudes larger than the visualization zone (≈ 3 mm) to indicate perfect light quality.[35] The relative position between light and cuvette could be adjusted by a three-axis displacement platform. Room temperature was controlled as 22 °C with 0.5 °C uncertainty.

Before a new test, the cuvette and nanofluid were sufficiently cooled to room temperature, ensuring similar conditions for each run. The laser was triggered with well-controlled E_l and f_l. Laser power $P = f_l E_l$ was measured by a power meter (15A-PH-DIF-18, OPHIR) with an uncertainty of 5%. An infrared camera (ImageIR 5380, InfraTec) measured pool liquid temperature with a spatial resolution of 30 µm and a temperature resolution of 0.02 °C. The recording speed was 100 Hz, which was sufficiently fast to capture the slow transition of pool liquid temperatures.

This measurement system included a synchronizer to ensure the simultaneous function of a laser device and a high-speed camera (MotionPro Y4, IDT). The synchronizer was triggered after steady oscillation of the system was reached. The high-speed camera recorded bubble images with a spatial resolution of 2.71 µm. Careful attention was paid on the selection of laser parameters and recording rate of the high-speed camera. Four parameters are involved in the synergy between laser and camera (see Figure 9c,d). The synchronizer had a synchronous error δt_s of 20 ns, behaving fast response. For laser, the delay time was $\delta t_d = 1$ µs and the pulse duration time was $\delta t_l = 180$ ns. For the camera, the exposure time was $\delta t_e = 200$ µs. Because δt_s, δt_d, and δt_l are at least two magnitudes shorter than δt_e, there should be a bubble image taken during pulse duration. Figure 9d presents the measurement principle for an example case with specific f_l and f_r. The exposure time of camera decreases when the recording frequency of camera increases. To ensure more images taken during one laser pulse, f_r should be several times of f_l. For example, $f_r = 2500$ Hz was used for $f_l = 500$ Hz.

Gold chloride hydrate (HAuCl$_4$, Au $\geq$ 49%, Aladdin China) and trisodium citrate (Na$_3$C$_6$H$_5$O$_7$, 99.8%, Sigma–Aldrich, USA) were the two materials to prepare nanofluid. Mixing and reacting of the two materials in a boiling water formed the nanofluid,[36] whose stabilization was enhanced by ultrasonic oscillation. The NPs' image, size distribution, τ_λ and $I_{a,0\sim I_a}/I_0$ are shown in Figure S1 (Supporting Information), where τ_λ is the transmittance, $I_{a,0\sim I_a}$ is the absorbed light energy, and I_0 is the incident intensity. NPs behave a narrow size distribution to have an average diameter $d_{p,ave} = 17.13$ nm. τ_λ reaches a minimum at $\lambda = 520$ nm, very close to the laser wavelength $\lambda = 527$ nm. Hence, the light energy absorption is enhanced due to the NPs' plasmonic effect.[34] $I_{a,0\sim I_a}/I_0$ characterizes the absorption and decay characteristics when light penetrates a liquid. For the 200 ppm nanofluid, this measurement showed that 80% of the light energy is absorbed within an optical length l_a of 3.5 mm, the remaining 20% is available beyond the 3.5 mm length. The parameters, instruments, and uncertainties are summarized in Table S1 (Supporting Information).

Supporting Information

Supporting Information is available from the Wiley Online Library or from the author.

Conflict of Interest

The authors declare no conflict of interest.

[1] A. Ashkin, *Science* **1980**, *210*, 1081.
[2] J. A. Boales, F. Mateen, P. Mohanty, *Sci. Rep.* **2017**, *7*, 16056.

[3] P. F. Hopkins, E. Quataert, N. Murray, *Mon. Not. R. Astron. Soc.* **2012**, *421*, 3522.

[4] N. Murray, E. Quataert, T. A. Thompson, *Astrophys. J.* **2010**, *709*, 191.

[5] C. W. Qiu, L. M. Zhou, *Light: Sci. Appl.* **2018**, *7*, 86.

[6] A. Henig, S. Steinke, M. Schnurer, T. Sokollik, R. Horlein, D. Kiefer, D. Jung, J. Schreiber, B. M. Hegelich, X. Q. Yan, J. Meyer-ter-Vehn, T. Tajima, P. V. Nickles, W. Sandner, D. Habs, *Phys. Rev. Lett.* **2009**, *103*, 4.

[7] A. Ashkin, J. Dziedzic, *Phys. Rev. Lett.* **1973**, *30*, 139.

[8] A. Casner, J.-P. Delville, *Opt. Lett.* **2001**, *26*, 1418.

[9] D. Baigl, *Lab Chip* **2012**, *12*, 3637.

[10] S. G. Kandlikar, *J. Heat Transfer* **2001**, *123*, 1071.

[11] B. Zhu, J. Xu, C. Yan, J. Xie, *Int. J. Heat Mass Transfer* **2020**, *148*, 119080.

[12] H. Šípová-Jungová, D. Andrén, S. Jones, M. Käll, *Chem. Rev.* **2020**, *120*, 269.

[13] X. Yan, G. Liu, J. Xu, S. Wang, *Sol. Energy* **2018**, *173*, 665.

[14] F. Winterer, C. M. Maier, C. Pernpeintner, T. Lohmuller, *Soft Matter* **2018**, *14*, 628.

[15] M. Ishii, N. Zuber, *AIChE J.* **1979**, *25*, 843.

[16] K. Iizuka, *Geometrical Optics*, Springer, Berlin **2019**.

[17] C. Zhao, Y. Xie, Z. Mao, Y. Zhao, J. Rufo, S. Yang, F. Guo, J. D. Mai, T. J. Huang, *Lab Chip* **2014**, *14*, 384.

[18] Y. Nishimura, K. Nishida, Y. Yamamoto, S. Ito, S. Tokonami, T. Iida, *J. Phys. Chem. C* **2014**, *118*, 18799.

[19] R. Manica, E. Klaseboer, D. Y. Chan, *Langmuir* **2015**, *31*, 6763.

[20] S. Ramachandran, C. B. Sobhan, G. P. Peterson, *Int. J. Heat Mass Transfer* **2020**, *147*, 118925.

[21] F.-C. Wang, H.-A. Wu, *Soft Matter* **2013**, *9*, 5703.

[22] Y. Min, M. Akbulut, K. Kai, Y. Golan, J. Israelachvili, *Nat. Mater.* **2008**, *7*, 527.

[23] Q. Wang, W. Yao, X. Quan, P. Cheng, *Int. Commun. Heat Mass Transfer* **2018**, *95*, 63.

[24] J. Xie, J. Xu, Q. Liu, X. Li, *Adv. Mater. Interfaces* **2017**, *4*, 1700684.

[25] M. Wang, C. Zhao, X. Miao, Y. Zhao, J. Rufo, Y. J. Liu, T. J. Huang, Y. Zheng, *Small* **2015**, *11*, 4423.

[26] L. Jiang, D. Erickson, *Small* **2013**, *9*, 107.

[27] G. L. Liu, J. Kim, Y. Lu, L. P. Lee, *Nat. Mater.* **2006**, *5*, 27.

[28] Y. K. Suh, S. Kang, *Micromachines* **2010**, *1*, 82.

[29] A. D. Stroock, S. K. W. Dertinger, A. Ajdari, I. Mezić, H. A. Stone, G. M. Whitesides, *Science* **2002**, *295*, 647.

[30] T. S. Zhao, P. Cheng, *Appl. Sci. Res.* **1997**, *59*, 11.

[31] B. Yuan, Y. Zhang, L. Liu, J. Wei, Y. Yang, *Int. J. Heat Mass Transfer* **2020**, *146*, 118825.

[32] J.-a. Lv, Y. Liu, J. Wei, E. Chen, L. Qin, Y. Yu, *Nature* **2016**, *537*, 179.

[33] J. R. Vélez-Cordero, M. G. P. Zúñiga, J. Hernández-Cordero, *Lab Chip* **2015**, *15*, 1335.

[34] J. Xu, X. Yan, G. Liu, J. Xie, *Nano Energy* **2019**, *57*, 791.

[35] O. V. Angelsky, A. Y. Bekshaev, P. P. Maksimyak, A. P. Maksimyak, S. G. Hanson, S. M. Kontush, *Opt. Express* **2017**, *25*, 5232.

[36] G. Frens, *Nat. Phys. Sci.* **1973**, *241*, 20.